

Topological states and interplay between spin-orbit and Zeeman interactions in a spinful Su-Schrieffer-Heeger nanowire

Zhi-Hai Liu ^{1,*}, O. Entin-Wohlman ², A. Aharony ², J. Q. You,³ and H. Q. Xu^{1,4,†}

¹*Beijing Key Laboratory of Quantum Devices, Key Laboratory for the Physics and Chemistry of Nanodevices, Department of Electronics, Peking University, Beijing 100871, China*

²*School of Physics and Astronomy, Tel Aviv University, Tel Aviv 69978, Israel*

³*Interdisciplinary Center of Quantum Information and Department of Physics, Zhejiang University, Hangzhou 310027, China*

⁴*Beijing Academy of Quantum Information Sciences, Beijing 100193, China*



(Received 20 April 2021; accepted 26 July 2021; published 6 August 2021)

The interplay between the spin-orbit and Zeeman interactions acting on a spinful Su-Schrieffer-Heeger model is studied based on an InAs nanowire subjected to a periodic gate potential along the axial direction. It is shown that a nontrivial topological phase can be achieved by regulating the confining-potential configuration. In the absence of the Zeeman field, we prove that the topology of the chain is not affected by the Rashba spin-orbit interaction due to the persisting chiral symmetry. The energies of the edge modes can be manipulated by varying the magnitude and direction of the external magnetic field. Remarkably, the joint effect of the two spin-related interactions leads to novel edge states that appear in the gap formed by the anticrossing of the bands of a finite spinful dimerized chain, and can be merged into the bulk states by tilting the magnetic-field direction.

DOI: [10.1103/PhysRevB.104.085302](https://doi.org/10.1103/PhysRevB.104.085302)

I. INTRODUCTION

A foremost feature of topological insulators is the appearance of metallic edge (or surface) modes inside the insulating bulk energy band gap [1,2]. These zero-energy edge states, which reside at the boundary of a topological system [3], are protected by the chiral symmetry of the bulk system. In reality this symmetry is often broken. It is therefore of great importance to investigate the bulk-edge relationship under such circumstances.

The simplest model which captures the topological phase transition as a function of the Hamiltonian parameters is the one-dimensional Su-Schrieffer-Heeger (SSH) model [4]. This prototype offers an excellent platform for simulating more intricate topological systems [5–7], and exploring physical effects caused by non-Hermitian Hamiltonians [8–12]. Experimentally, besides explaining the physics of polyacetylene [5], topological phases as found in the SSH model have been realized in certain synthetic dimerized systems, such as optical superlattices [13], ultracold atoms [14–16], micropillar and other photonic crystals [17–20], atomically engineered superlattices [21], and graphene nanoribbons [22,23]. However, studies of the effect of time-reversal symmetry breaking on a fermionic dimerized chain are still rather scarce. Even more surprising is the confusion in the literature regarding the effects of the spin-orbit interaction. Spin-orbit interactions are of paramount importance in developing topological insulators and superconductors [24,25]. Several attempts to investigate the impacts of spin-orbit interactions on the topological features of the SSH model have been reported, see for instance

Refs. [26,27]. Regrettably, these papers fail to incorporate correctly the time-reversal symmetry of spin-orbit interaction in their model Hamiltonians and, in fact, consider the effect of a Zeeman field, which breaks time-reversal symmetry. The correct inclusion of the spin-orbit-induced spin flips in tunneling Hamiltonians is via the (time-reversal symmetric) Aharonov-Casher effect [28], which appears as phase factors that dominate the tunneling amplitudes of the dimerized system [29,30].

Recently, the topological phase of the spinful Su-Schrieffer-Heeger configuration has been approached experimentally [20,31], by studying the edge modes of a photonic dimerized chain lacking time-reversal symmetry. In particular, Ref. [20] which studies topological modes in micropillar lattices (the bosonic analog of the SSH model) relates the breaking of time-reversal symmetry to a k -dependent effective magnetic field acting on the polarization of the photons. It is then observed that the edge states do not reside in the midgap, as predicted for bosonic systems without chiral symmetry [32]. The analysis of edge modes in a fermionic topological system where time-reversal and chiral symmetries are not always obeyed thus seems to be quite timely.

II. MODEL AND EFFECTIVE HAMILTONIAN

We present a study of the joint effect of spin-orbit interaction (SOI) and an external magnetic field on the topological features of an electron dimerized chain. Our analysis is based on a realistic Hamiltonian of an InAs nanowire, rendering the conclusions amenable to experimental verifications. Specifically, the sublattice degrees of freedom of the chain are represented by the localized orbitals of two quantum dots defined by the periodically arranged gate potentials along the wire axis, as shown in Figs. 1(a) and 1(b). Under the

*zhihailiu@pku.edu.cn

†hqxu@pku.edu.cn

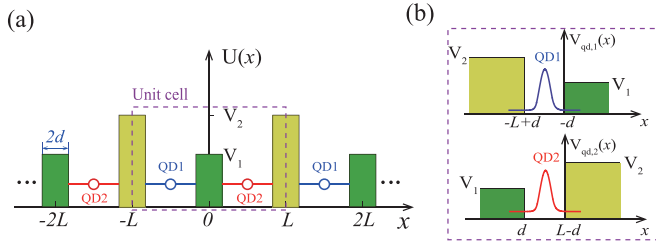


FIG. 1. (a) A semiconductor wire subjected to gate potentials V_1 and V_2 arranged periodically along the axial direction x , to form a double quantum-dot chain. The length of the unit cell is $2L$, and $2d$ is the width of each potential wall. (b) The local potentials $V_{\text{qd},1}(x)$ and $V_{\text{qd},2}(x)$ that define two quantum dots (QD1 and QD2) within each unit cell, and the lowest orbital on each dot. Our analysis also applies for the case $V_1 > V_2$ (not shown).

interplay between the Zeeman and spin-orbit interactions, the strategy in constructing a trackable model for the semiconductor nanowire is based on the Bloch spectrum of its full Hamiltonian which is used to obtain a discretized form, amenable to the analysis of topological features. This approach, whose validity is demonstrated below, allows us to determine the specific form of the spinful discrete Hamiltonian, for the gated InAs nanowire.

Assuming that the magnetic field is applied in the y - z plane along $\hat{\zeta}$, $\mathbf{B} = B\{0, \cos(\theta), \sin(\theta)\} \equiv B\hat{\zeta}$, and the spin-orbit interaction is of the Rashba type, yielding an effective magnetic field along y , the Hamiltonian of the InAs nanowire reads [33]

$$H = \frac{p^2}{2m_e} - V_c + U(x) + \alpha p\sigma_y + \frac{\Delta_z}{2}\sigma_z. \quad (1)$$

Here m_e is the electron's effective mass, $p = -i\hbar\partial/\partial x$ is the momentum, V_c denotes the off-set chemical potential, $U(x)$ is the periodic gate potential, α corresponds to the strength of the Rashba SOI, and $\Delta_z = g\mu_B B$ is the Zeeman splitting, with g being the Landé factor (μ_B is the Bohr magneton). The spin-orbit interaction can also be quantified by the length $x_{\text{so}} = \hbar/(m_e\alpha)$. In Eq. (1), $\sigma_{\zeta} = \hat{\sigma} \cdot \hat{\zeta}$, with the Pauli matrices $\hat{\sigma} = (\sigma_x, \sigma_y, \sigma_z)$. The orbital effect of the magnetic field is ignored due to the strong confining potential along the direction normal to \mathbf{B} , which enables the averaging out the vector-potential terms in the Landau gauge [33]. The periodic potential creates, in each unit cell, two quantum dots (QD1 and QD2), confined by the potentials $V_{\text{qd},1}(x)$ and $V_{\text{qd},2}(x)$, such that

$$V_{\text{qd},1}(x) = V_1\Theta(d+x) + V_2\Theta(d-L-x) \quad (2)$$

with $-L \leq x \leq L$, where $V_{\text{qd},2}(x) = V_{\text{qd},1}(-x)$ and $2L$ is the length of the unit cell [$\Theta(x)$ is the Heaviside function]. $V_{1,2}$ are two separate potential barriers (see Fig. 1), whose width is $2d$. All the calculations below are based on a realistic InAs nanowire, for which $m_e = 0.023m_0$ (m_0 is the free electron mass), the lattice constant is $2L = 120$ nm, the Landé g factor is $g = 15$ [34], the spin-orbit length is about $x_{\text{so}} = 180$ nm [35], and the gate potentials, of widths $2d = 20$ nm, obey $V_1 + V_2 = 40$ meV [36].

The lowest Zeeman-split levels of the QD's are used to construct a discrete Hamiltonian of the double quantum-dot

chain

$$H_T = \sum_n (a_n^\dagger t_{\text{in}} b_n + a_{n+1}^\dagger t_{\text{ex}} b_n + \text{H.c.}) + \frac{\Delta_z}{2} \sum_n (a_n^\dagger \sigma_z a_n + b_n^\dagger \sigma_z b_n), \quad (3)$$

where n is the index of the unit cell and $a_n = \{a_{n\uparrow}, a_{n\downarrow}\}$ and $b_n = \{b_{n\uparrow}, b_{n\downarrow}\}$ are the spinors for the quasipin states on QD1 and QD2, respectively. Under the joint effect of the spin-orbit and Zeeman interactions, the intra-/intercell tunneling amplitudes $t_{\text{in/ex}}$ are matrices in spin space,

$$t_{\text{in/ex}} = t_{\text{in/ex},0} \exp[i\varphi_{\text{in/ex}}(\hat{v}_{\text{in/ex}} \cdot \hat{\sigma})]. \quad (4)$$

The phase factors $\varphi_{\text{in/ex}} \propto L/x_{\text{so}}$ and the unit vectors $\hat{v}_{\text{in/ex}} = \{\sin(\vartheta_{\text{in/ex}}), 0, \cos(\vartheta_{\text{in/ex}})\}$ are determined by the relative angle θ between the directions of the Zeeman field and the one induced by the SOI [37]. Details are given in Appendix A. Notably, the spin space for defining the Pauli matrices $\sigma_{x,y,z}$ in Eqs. (3) and (4) consists of the two lowest Zeeman splitting levels on each dot and does not coincide with that defining the spin operators in Eq. (1). Therefore, the Zeeman interaction in Eq. (1) appears as a σ_z term in Eq. (3).

In the absence of the Zeeman and spin-orbit interactions, i.e., $\Delta_z = 0$ and $\varphi_{\text{in/ex}} = 0$, the spinless version of H_T describes the well-known Su-Schrieffer-Heeger model [4,38] $H_{T,0} = \sum_n (t_{\text{in},0} a_n^\dagger b_n + t_{\text{ex},0} a_{n+1}^\dagger b_n + \text{H.c.})$, with a_n and b_n representing the annihilation operators for the two-site unit cell. As is well known, this model leads to a topological transition depending on the degree of dimerization, denoted as t_- with

$$t_{\pm} = t_{\text{ex},0} \pm t_{\text{in},0}, \quad (5)$$

which for the InAs nanowire t_- is determined by $\Delta V = V_1 - V_2$. Figures 2(a) and 2(b) exhibit comparisons between the spinless Bloch spectra obtained from the ‘‘exact’’ Hamiltonian in Eq. (1), and from the approximated one in Eq. (3), which show that the spectra of the latter follows those of the former quite faithfully [39]. A further support for the compatibility of our tight-binding description for a realistic InAs nanowire emanates from the fact that the band gap closes at the critical point $\Delta V = 0$. Specifically, the ‘‘exact’’ Bloch spectrum of the synthetic lattice is derived exploiting periodic boundary conditions of the Bloch functions in a unit cell, see Appendix B. Moreover, using the cell-periodic Bloch functions $u_k(x) = u_k(x + 2L)$, one obtains the Zak phase $\varphi_{\text{zak}} = i \int_{-\pi}^{\pi} \int_{-L}^L u_k^\dagger(x) \frac{\partial}{\partial k} u_k(x) dx dk$ [40,41]. The integration is carried out by the discretization method introduced in Ref. [42]. It is found that the Zak phase of each Bloch band depends on the confinement configuration such that $\varphi_{\text{zak}} = 0$ for $\Delta V < 0$, and $\varphi_{\text{zak}} = \pi$ for $\Delta V > 0$, in full agreement with the one derived from the tight-binding description of the SSH model [38], based on the dependence of the dimerization degree on the potential difference.

The Bloch bands of the spinful Hamiltonian (1) are displayed in Figs. 2(c) and 2(d) by the dashed curves. The ones belonging to the discretized version, Eq. (3), are shown as solid curves. Again, a good agreement between the two spectra is obtained. Note in particular the closing of the gap at $k = 0$ and $k = \pm\pi$ for zero magnetic field, similarly to the

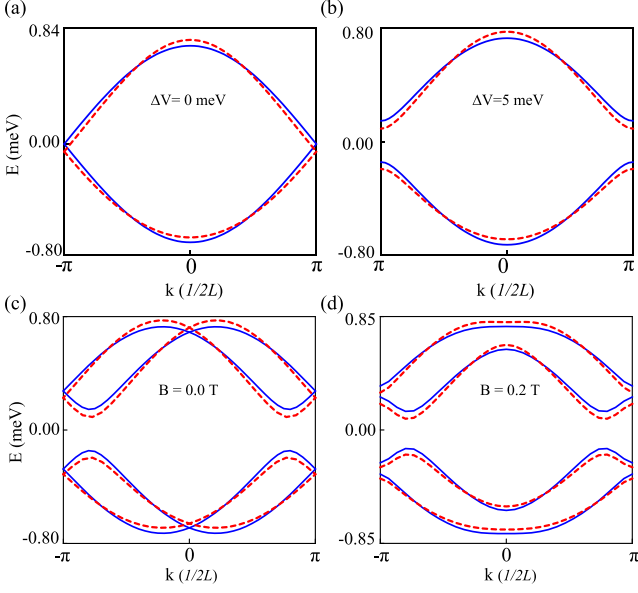


FIG. 2. [(a) and (b)] The energy spectra of the spinless InAs double quantum-dot chain versus the wave vector k for different potential differences ΔV . (c) The Bloch spectrum of the spinful InAs chain at zero Zeeman field ($B = 0$), for $\Delta V = 5.0$ meV and $x_{\text{so}} = 180$ nm. (d) The same as (c), for $B = 0.2$ T tilted by $\theta = 0.5\pi$ in the y - z plane. The dashed (red) curves depict the energy levels of the Bloch spectrum, calculated from the continuous Hamiltonian (1), and the solid (blue) curves are derived from the discrete Hamiltonian (3).

spinless SSH model. This results from the chiral symmetry of the Rashba interaction (see below).

III. TOPOLOGICAL EDGE MODES FOR BROKEN CHIRAL SYMMETRY

By analogy with the spinless SSH model, the nontrivial topological phase is characterized by the appearance, at $\Delta V > 0$, of two zero-energy edge modes in a finite chain of N sites with open boundary conditions, see Figs. 3(a) and 3(b). In the thermodynamic limit ($N \rightarrow \infty$), these two zero-energy edge modes are separately located on either side of the chain and hence each belongs to a different sublattice [3,43]. For an open short chain comprising 20 sites, the separated edge modes are coupled to each other; the hybridized edge modes can be written as $|E_{\pm}\rangle = \sum_{n=1}^{20} (A_n a_n^{\dagger} \pm B_n b_n^{\dagger})|0\rangle$, where $|0\rangle$ is the vacuum state and A_n and B_n are the probability amplitudes on the two sites of the n th unit cell. In this case, the spatial density distribution of the two edge modes at the n th site is $P_n = |A_n|^2 + |B_n|^2$ and it depends on the potential difference ΔV . As seen in Fig. 3(b), the larger ΔV is, the more localized is the edge state, due to the accompanying enhanced dimerization strength [44].

Interestingly, the presence of the spin-orbit coupling does not cause qualitative changes in this picture. At zero Zeeman field, we find zero-energy edge modes. [Note that the energy spectrum of an open spin-orbit-active chain is a doubled copy of that of the spinless chain shown in Fig. 3(a).] In fact, these zero-energy modes are protected by the chiral symmetry of the

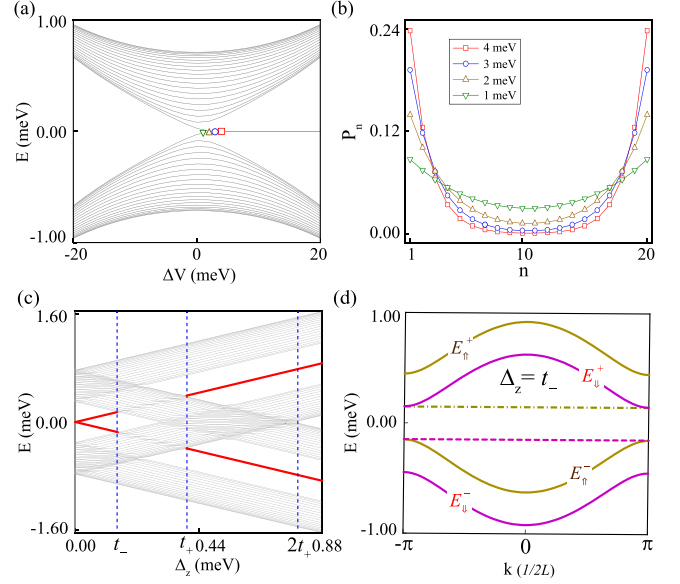


FIG. 3. (a) The energy spectrum of a finite spinless chain versus ΔV . The spatial density distributions of one spinless edge mode, P_n , for different values of ΔV , as indicated by the symbols in panel (a), are displayed in (b). (c) The energy spectrum of a finite chain of 20 sites versus Δ_z for $\Delta V = 10$ meV, $\theta = 0.5\pi$, and zero spin-orbit coupling. The emergence of the Zeeman-split edge states is indicated by the thick (red) lines. (d) The Bloch spectrum of the semiconductor chain as a function of k with $\Delta_z = t_-$, $\Delta V = 10$ meV, $\theta = 0.5\pi$, and zero spin-orbit coupling. Besides, the energy values of the spin-up and spin-down edge states are indicated by the (yellow) dash-dotted and (purple) dashed lines, respectively.

discrete Hamiltonian (3) for $\Delta_z = 0$: $\mathcal{C}H_T\mathcal{C}^{-1} = H_T$, where the chiral symmetry operator is $\mathcal{C} = \mathcal{TP}$. Here \mathcal{T} is the time-reversal operator and \mathcal{P} is the particle-hole operator, which for a spinful bipartite lattice is defined by $\mathcal{P}a_{\uparrow/\downarrow}\mathcal{P}^{-1} = \pm a_{\downarrow/\uparrow}^{\dagger}$ and $\mathcal{P}b_{\uparrow/\downarrow}\mathcal{P}^{-1} = \mp b_{\downarrow/\uparrow}^{\dagger}$.

The Zeeman interaction which breaks time-reversal symmetry lifts the chiral symmetry. In the absence of the spin-orbit interaction (i.e., for $\varphi_{\text{in/ex}} = 0$), the spinful Hamiltonian H_T is separated into two independent models for each spin projection, $H_T = H_{\uparrow} + H_{\downarrow}$ with

$$H_{\tau=\uparrow/\downarrow} = \sum_n (t_{\text{in},0} a_{n\tau}^{\dagger} b_{n\tau} + t_{\text{ex},0} a_{n+1\tau}^{\dagger} b_{n\tau} + \text{H.c.}) \pm \frac{\Delta_z}{2} \sum_n (a_{n\tau}^{\dagger} a_{n\tau} + b_{n\tau}^{\dagger} b_{n\tau}). \quad (6)$$

Structurally, $H_{\uparrow/\downarrow}$ can be mapped onto an effective SSH model with a finite on-site energy $\pm\Delta_z/2$. It follows that in principle there exist two edge states in each spin sector for $t_- > 0$, see Eq. (5). However, there is a caveat: Since each spin-polarized edge mode can merge into the bulk states pertaining to the other spin direction, which happens for $t_- \leq \Delta_z \leq t_+$, the available Zeeman splittings for which spin-polarized edge modes can appear is restricted, as shown in Fig. 3(c).

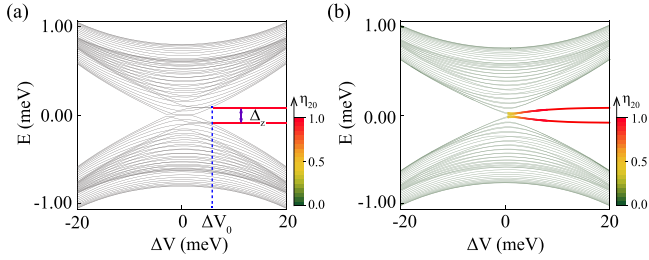


FIG. 4. (a) The energy spectrum of a finite spinful InAs chain versus ΔV for $B = 0.2$ T and $\theta = \pi/2$ and in the absence of the SOI. The edge states appearing in the band gap are indicated by the thick (red) lines. (b) The same as in (a) but in the presence of the SOI. The coefficient η_{20} characterizes the degree of confinement of the edge states in a 20 site chain.

To further illustrate this point, we examine the Bloch spectrum in the absence of the SOI,

$$E_{\uparrow}^{\pm}(k) = \frac{\Delta_z}{2} \pm \sqrt{t_{\text{in},0}^2 + t_{\text{ex},0}^2 + 2t_{\text{in},0}t_{\text{ex},0} \cos k} \quad (7)$$

$$E_{\downarrow}^{\pm}(k) = -\frac{\Delta_z}{2} \pm \sqrt{t_{\text{in},0}^2 + t_{\text{ex},0}^2 + 2t_{\text{in},0}t_{\text{ex},0} \cos k}.$$

For a zero magnetic field, the energies of the edge states vanish; when this field is active and the edge states become spin polarized, their respective energies are $\varepsilon_{\uparrow/\downarrow} = \pm \Delta_z/2$. The energy of the spin-up edge state, ε_{\uparrow} , intersects the upper Bloch band $E_{\downarrow}^+(k)$ for $t_- \leq \Delta_z \leq t_+$. This conclusion also pertains to the intersection between ε_{\downarrow} and $E_{\uparrow}^-(k)$, as depicted in Fig. 3(d). As a result, the intersection is reflected by the coalescence of the bulk and edge states, as seen in Fig. 3(c).

For a Zeeman energy such that $\Delta_z < t_+$, the edge states appear above a certain value of the dimerization strength, $t_- > \Delta_z$, as reflected by the threshold value, denoted ΔV_0 in Fig. 4(a). This condition disappears in the presence of the SOI, as seen in Fig. 4(b), indicating that there is no further requirement on the dimerization strength in the nontrivial topological phase, i.e., $\Delta V > 0$. This feature can be understood by referring to the spin-orbit-active qubit discussed in Ref. [45]. The Landé g factor in the presence of the SOI, and consequently Δ_z , are reduced by a SOI-dependent factor $f = \exp[-x_0^2/x_{\text{SO}}^2]$ [45], where x_0 is the localization length of the edge mode. In fact, x_0 is correlated with the probability density distribution of the edge state $\tilde{P}_n = \sum_{\tau=\uparrow,\downarrow} [|A_{n,\tau}|^2 + |B_{n,\tau}|^2]$, where $A_{n,\tau}$ and $B_{n,\tau}$ are the amplitudes of the quasispin states on the QD1 and QD2, respectively. One may characterize the degree of confinement to the edges by introducing the measure (pertaining to a chain comprising 20 sites) $\eta_{20} = \sum_{n=1}^3 \tilde{P}_n + \sum_{n'=18}^{20} \tilde{P}_{n'}$. As portrayed in Fig. 4(b), η_{20} is reduced as ΔV is decreased, implying that the localization length is lengthened. As large x_0 's are realized at small ΔV 's this explains the results in that regime.

In the presence of a Zeeman field, the energies of the two doubly degenerate edge modes shown in Figs. 4(a) and 4(b) are split and localized symmetrically around zero energy, since the Hamiltonian obeys particle-hole symmetry, $\mathcal{P}H_T\mathcal{P}^{-1} = H_T$. Therefore, in order to facilitate the following analysis, we only focus on the variations of the upper energy

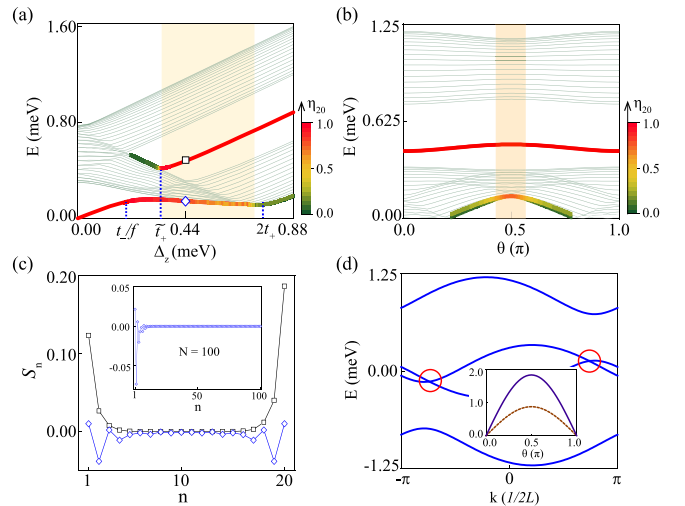


FIG. 5. (a) The positive energy spectrum of a finite spin-orbit-active chain of 20 sites versus the Zeeman splitting, with $\Delta V = 10$ meV and $\theta = 0.5\pi$. (b) The positive energy spectrum of the same chain versus the tilting angle θ of \mathbf{B} in the y - z plane for $\Delta_z = 0.44$ meV and $\Delta V = 10$ meV. Also shown are the (yellow) shadowed regions where there exist four pairs of edge modes whose degree of confinement is characterized by the coefficient η_{20} . (c) The spin-density distributions, S_n , of the two edge modes marked by a square and a diamond in panel (a). Moreover, for a discrete chain comprising of 100 sites, the spin-density distribution of the new edge mode [corresponding to the diamond in panel (a)] is further exemplified in the inset. (d) The Bloch spectrum of the spin-orbit-active chain versus k for $\Delta V = 10$ meV, $\Delta_z = 0.44$ meV, and $\theta = 0$. In this case, the anticrossing gap accommodating the spin-mixed edge states completely disappears, as indicated by the red circles. In addition, the inset shows the dependence of the two spin-flip tunneling amplitudes (in meV units) on θ , with the (purple) solid and (yellow) dashed curves representing the inter- and intracell tunneling amplitudes, $|t'_{\text{ex}}|$ and $|t'_{\text{in}}|$, respectively.

levels under different conditions. For a fixed value of ΔV the precondition for the appearance of the spin edge states is modified under the joint effect of the spin-orbit and Zeeman interactions. Because the energies of the Zeeman-split edge modes are modified by the SOI-induced factor f , the available range of Δ_z near zero magnetic field which supports edge modes is changed to $\Delta_z < t_-/f$, with $f \simeq 0.8$ for $\Delta V = 10$ meV, see Fig. 5(a).

The condition for the emergence of edge states at large magnetic fields, $\Delta_z > t_+$, is also modified in the presence of the SOI. While in the absence of SOI, the edge modes are the eigenvectors of σ_z separated by Δ_z , they become coupled by the spin-flip tunneling matrix elements, $t'_{\text{in/ex}}$, induced by the SOI [see Eq. (4)]. The resulting edge states can be explained by confining the discussion to the thermodynamic limit. Exploiting the orthonormal basis of σ_z , the Hamiltonian (3) is approximated by

$$H_T = \begin{pmatrix} \frac{\Delta_z}{2} & t' \\ t' & -\frac{\Delta_z}{2} \end{pmatrix}, \quad (8)$$

where $t' = \sqrt{|t'_{\text{in}}|^2 + |t'_{\text{ex}}|^2}$ represents the spin-flip coupling. The two eigenvalues of Eq. (8) are the modified energies of

the quasispin edge modes. The lower bound for their existence is $\tilde{t}_+ = \sqrt{t_+^2 - 4t^2}$. For $\Delta_z < \tilde{t}_+$, the quasispin edge modes are merged into the bulk states, as reflected by the sharp decrease of the confinement coefficient η_{20} shown in Fig. 5(a). The energies of these Zeeman-split edge states depend on the tilting angle θ of the magnetic field as shown in Fig. 5(b) and hence can be varied in experiment.

Remarkably, there appear additional edge modes for Zeeman splittings obeying $t_-/f \leq \Delta_z < 2t_+$, see Fig. 5(a), a range which is “forbidden” in Fig. 3(c). These modes result from the interplay between the Zeeman and spin-orbit interactions. They reside below the anticrossing gap induced by the spin-flip tunneling matrix elements in Eq. (4): The crossing of the Bloch bands $E_{\uparrow}^-(k)$ and $E_{\downarrow}^+(k)$ in momentum space is lifted by these spin-flip amplitudes, and a gap (“anticrossing gap”) is open. Indeed, introducing those as perturbations on the energy bands in Eqs. (7), one observes that the crossing, and simultaneously the gap opened by the spin-flip terms, disappear for $\Delta_z > 2t_+$. Hence, we deduce that these extra edge modes amalgamate with the bulk states for a Zeeman splitting smaller than the critical value, $2t_+$. This is reflected by the variation of η_{20} shown in Fig. 5(a). Numerically, a mode (of a 20 site chain) can be considered as an edge state for, say, $\eta_{20} > 0.5$, and the mergence of the new edge states into the bulk is verified by this criterion, correspondingly.

As compared to the Zeeman-split (higher energy) edge modes depicted in Fig. 5(a), the energy eigenvalues of these new edge states are insensitive to the increase of the Zeeman splitting due to the high degree of spin mixing. For this end, Fig. 5(c) displays the distributions of the spin density $S_n = \frac{1}{2}[|A_{n,\uparrow}|^2 + |B_{n,\uparrow}|^2 - |A_{n,\downarrow}|^2 - |B_{n,\downarrow}|^2]$, for the two edge modes illustrated in Fig. 5(a). Evidently, the new edge state (marked by the diamond) is distinguished from the spin-resolved edge mode (indicated by the square) by its small spin-density probability S_n . Similarly to the spatial distribution of the spinless edge modes shown in Fig. 3(b), the spin-density distribution of each spinful edge mode is split into two segments for an open short discrete chain comprising of 20 sites, see Fig. 5(c). Analogously, because the coupling between the two presumably separated edge modes (located in different sides of the chain) is negligible in the thermodynamic limit, the extra edge mode can only reside in either side of the chain, as indicated by the spin-density distribution S_n shown in the inset of Fig. 5(c) for $N = 100$.

Hence, the total number of the edge modes can be doubled when $\tilde{t}_+ < \Delta_z < 2t_+$, as indicated in Fig. 5(a). However, in contrast to the Zeeman-split edge states, the spin-mixed edge modes can be merged into the bulk states by tilting the magnetic field in the y - z plane, as shown in Fig. 5(b), due to the dependence of the tunneling amplitudes on the tilting angle, see Eq. (4). In particular, for $\theta = 0$, the spin of the dimerized chain is conserved, $\vartheta_{\text{in/ex}} = 0$ and $t'_{\text{in/ex}} = 0$, and the gap opened due to the anticrossing of the spin-resolved energy levels completely disappears, as shown in Fig. 5(d).

IV. CONCLUSIONS

Specifying to an InAs nanowire with strong Rashba spin-orbit interaction, we have shown that this interaction by itself does not affect the topology of a spinful Su-Schrieffer-Heeger

model, as opposed to the significant effects of spin-orbit interaction found in Refs. [20,26,27]. In the presence of an external magnetic field, we find that the joint effect of the spin-orbit and Zeeman interactions allows for a plethora of edge modes which are not protected by chiral symmetry. The edge states can be classified into two groups. The first includes the Zeeman-split edge states, and the second comprises the ones induced by the interplay between the two spin-related interactions appearing at a sufficiently large Zeeman splitting. Interestingly, these new states exist in the gap opened by the anticrossing of the energy bands and may merge into the bulk by tilting the magnetic-field direction. This remarkable observation can be examined experimentally using semiconductor nanowires [46–48] and graphene nanoribbons [21,23].

ACKNOWLEDGMENTS

This work is supported by the Ministry of Science and Technology of China through the National Key Research and Development Program of China (Grants No. 2017YFA0303304 and No. 2016YFA0300601), the National Natural Science Foundation of China (Grants No. 91221202, No. 91421303, No. 11874071, and No. 11934010), the Beijing Academy of Quantum Information Sciences (Grant No. Y18G22), and the Key-Area Research and Development Program of Guangdong Province (Grant No. 2020B0303060001). O.E.-W. and A.A. acknowledge support by the Israel Science Foundation (ISF), by the infrastructure program of Israel Ministry of Science and Technology under Contract No. 3-11173, and by the Pazy Foundation.

APPENDIX A: THE TIGHT-BINDING HAMILTONIAN OF THE MODEL SYSTEM

Here is outlined the derivation of the nearest-neighbor tight-binding Hamiltonian of our model. The derivation is based on the original Hamiltonian, Eq. (1) in the main text. The periodic gate potential there, $U(x)$, is viewed as composed of two alternating quantum dots, QD1 and QD2, as depicted in Fig. 6(a) and 6(b). Each quantum dot obeys the Hamiltonian

$$H_{1/2} = \frac{p^2}{2m_e} + V_{\text{qd},1/2}(x) + \alpha p \sigma_y + \frac{\Delta_z}{2} \sigma_z, \quad (\text{A1})$$

where α is the strength of the Rashba spin-orbit interaction, Δ_z is the Zeeman splitting, $\sigma_n = \hat{\sigma} \cdot \hat{\xi}$ with $\hat{\xi} = \{\cos \theta, \sin \theta\}$ being the direction vector of the external magnetic field and $\hat{\sigma}$ denotes the Pauli matrices, $\hat{\sigma} = \{\sigma_x, \sigma_y, \sigma_z\}$. The confining potentials that define the quantum dots are

$$V_{\text{qd},1}(x) = \begin{cases} V_1 & x \geq -d \\ 0 & -L + d \leq x < -d, \\ V_2 & x < -L + d \end{cases}$$

$$V_{\text{qd},2}(x) = \begin{cases} V_1 & x < d \\ 0 & d \leq x < L - d. \\ V_2 & x \geq L - d \end{cases} \quad (\text{A2})$$

We next solve for the energy eigenstates of the two dots using Eq. (A1). Moreover, in order to preserve the locality of the wave functions, we assume the electron energy eigenvalue

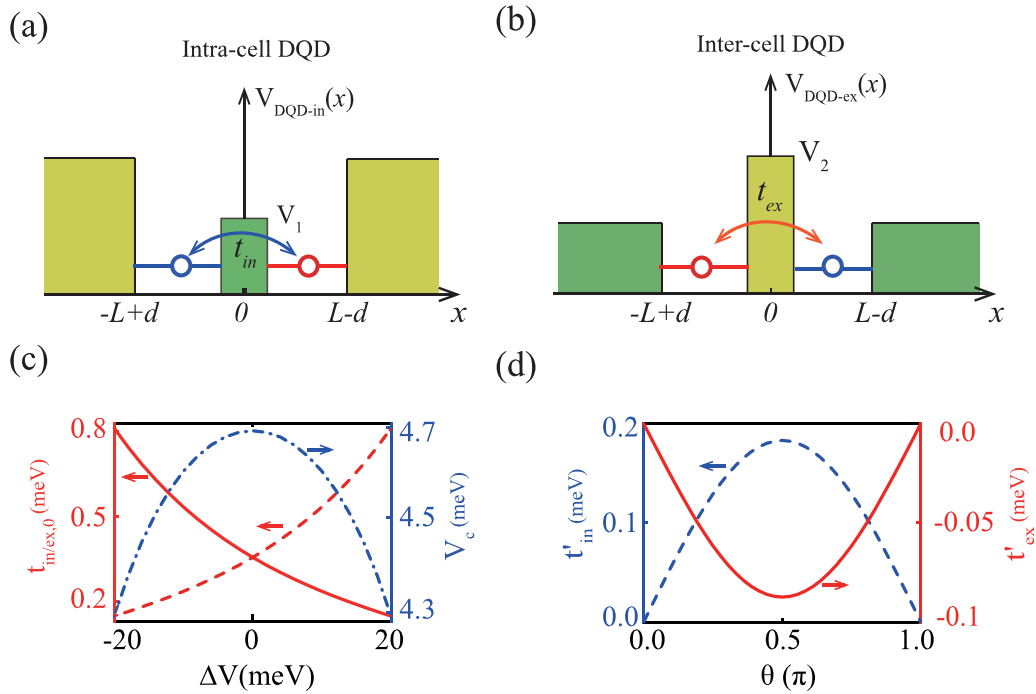


FIG. 6. (a) The spatial distribution of the confining potential $V_{\text{DQD-in}}(x)$ that determines the intracell tunneling amplitude within the double quantum-dot chain in the main text (see Fig. 1). (b) The confining potential $V_{\text{DQD-ex}}(x)$ that determines the intercell tunneling amplitude. (c) The intra-/intercell hopping amplitude of an InAs double quantum dot chain, $t_{\text{in/ex},0}$, as a function of the potential difference $\Delta V = V_1 - V_2$, with the periodic length $2L = 120$ nm and $d = 10$ nm. Here $t_{\text{in},0}$ ($t_{\text{ex},0}$) is denoted by the solid (dashed) line and the variations of the chemical potential V_c are displayed by the dash-dotted curve. (d) The intra- and intercell spin-flip tunneling amplitudes, t'_{in} and t'_{ex} , of the double-quantum-dot chain as functions of the tilting angle θ , with the potential difference $\Delta V = -10$ meV, the magnetic field strength $B = 1.0$ T, and the spin-orbit interaction scaled by $x_{\text{so}} \equiv \hbar/(m_e\alpha) = 180$ nm.

$E < \min\{V_1, V_2\}$. It is expedient to consider the Schrödinger equation pertaining to all three regions in Eq. (A2) by introducing

$$\tilde{H}_{\zeta=0,1,2}\psi_{\zeta}(x) = E\psi_{\zeta}(x). \quad (\text{A3})$$

Here ψ_{ζ} is the corresponding eigenfunction on each portion and

$$\tilde{H}_{\zeta} = \frac{p^2}{2m_e} + \alpha p\sigma_y + \frac{\Delta_z}{2}\sigma_{\zeta} + V_{\zeta}, \quad (\text{A4})$$

where $V_0 = 0$ and $V_{1,2}$ are given in Eqs. (A2). The eigenfunctions of \tilde{H}_{ζ} are spinors,

$$\psi_{\zeta}(x) = \exp(i\gamma_{\zeta}x) \begin{pmatrix} w_{\zeta} \\ d_{\zeta} \end{pmatrix}. \quad (\text{A5})$$

For a fixed value of E there exist four independent solutions to Eq. (A3), with the corresponding wave vectors $\gamma_{\zeta,\lambda=1,2,3,4}$

determined by the quartic equation

$$\left(\frac{\hbar^2\gamma_{\zeta}^2}{2m_e} + V_{\zeta} - E \right)^2 - \hbar^2\gamma_{\zeta}^2\alpha^2 - \Delta_z\hbar\gamma_{\zeta}\alpha\cos(\theta) - \frac{\Delta_z^2}{4} = 0. \quad (\text{A6})$$

The respective spinor components are

$$w_{\zeta,\lambda} = i\hbar\alpha\gamma_{\zeta,\lambda} + i\frac{\Delta_z}{2}\cos(\theta),$$

$$d_{\zeta,\lambda} = \frac{\hbar^2\gamma_{\zeta,\lambda}^2}{2m_e} + \frac{\Delta_z}{2}\sin(\theta) + V_{\zeta} - E. \quad (\text{A7})$$

In particular, when $\theta = \pi/2$, the expressions for the wave vectors can be derived analytically

$$\gamma_{\zeta,1/2} = \pm \sqrt{\frac{2m_e}{\hbar^2} \sqrt{E - V_{\chi} + m_e\alpha^2 + \sqrt{m_e^2\alpha^4 + 2m_e\alpha^2(E - V_{\chi}) + \Delta_z^2/4}}}$$

$$\gamma_{\zeta,3/4} = \pm \sqrt{\frac{2m_e}{\hbar^2} \sqrt{E - V_{\chi} + m_e\alpha^2 - \sqrt{m_e^2\alpha^4 + 2m_e\alpha^2(E - V_{\chi}) + \Delta_z^2/4}}}. \quad (\text{A8})$$

The convergence of the wave function at $x \rightarrow \infty$ requires the wave vectors to have $\text{Im}[\gamma_1] > 0$ for dot 1 and $\text{Im}[\gamma_2] > 0$ for dot 2. The convergence condition for $x \rightarrow -\infty$ is $\text{Im}[\gamma_2] < 0$ for dot 1 and $\text{Im}[\gamma_1] < 0$ for dot 2. Then, the energy eigenfunctions

of QD1 and QD2 can be written as

$$\Psi_1(x) = \sum_{\lambda=1}^4 c_{0,\lambda} [1 - \Theta(x+d)]\Theta(x+L-d)\psi_{0,\lambda}(x) + \Theta(x+d)[c_{1,1}\psi_{1,1}(x) + c_{1,4}\psi_{1,4}(x)] \\ + [1 - \Theta(x+L-d)][c_{2,2}\psi_{2,2}(x) + c_{2,3}\psi_{2,3}(x)] \quad (\text{A9})$$

$$\Psi_2(x) = \sum_{\lambda=1}^4 v_{0,\lambda} [1 - \Theta(x-L+d)]\Theta(x-d)\psi_{0,\lambda}(x) + [1 - \Theta(x-d)][v_{1,2}\psi_{1,2}(x) + v_{1,3}\psi_{1,3}(x)] \\ + \Theta(x-L+d)[v_{2,1}\psi_{2,1}(x) + v_{2,4}\psi_{2,4}(x)], \quad (\text{A10})$$

where $\Theta(x)$ is the Heaviside step function $\Theta(x) = \begin{cases} 0 & x \leq 0 \\ 1 & x > 0 \end{cases}$, the coefficients $c_{\zeta,\lambda}$ and $v_{\zeta,\lambda}$ are determined by the boundary conditions, i.e., from the continuity equations at $x_{1/3} = \mp d$ and $x_{2/4} = \mp L \pm d$. Using the explicit form for $V_{qd,1}(x)$ in Eq. (A2), the boundary conditions for the localized wave function on QD1 are [49]

$$\lim_{\epsilon \rightarrow 0} [\Psi_1(x_1 + \epsilon) - \Psi_1(x_1 - \epsilon)] = 0, \\ \lim_{\epsilon \rightarrow 0} [\Psi_1(x_2 + \epsilon) - \Psi_1(x_2 - \epsilon)] = 0,$$

$$\mathbf{M} = \begin{pmatrix} \psi_{0,1,1}(x_1) & \psi_{0,2,1}(x_1) & \psi_{0,3,1}(x_1) & \psi_{0,4,1}(x_1) \\ \psi_{0,1,2}(x_1) & \psi_{0,2,2}(x_1) & \psi_{0,3,2}(x_1) & \psi_{0,4,2}(x_1) \\ \psi_{0,1,1}(x_2) & \psi_{0,2,1}(x_2) & \psi_{0,3,1}(x_2) & \psi_{0,4,1}(x_2) \\ \psi_{0,1,2}(x_2) & \psi_{0,2,2}(x_2) & \psi_{0,3,2}(x_2) & \psi_{0,4,2}(x_2) \\ \gamma_{0,1}\psi_{0,1,1}(x_1) & \gamma_{0,2}\psi_{0,2,1}(x_1) & \gamma_{0,3}\psi_{0,3,1}(x_1) & \gamma_{0,4}\psi_{0,4,1}(x_1) \\ \gamma_{0,1}\psi_{0,1,2}(x_1) & \gamma_{0,2}\psi_{0,2,2}(x_1) & \gamma_{0,3}\psi_{0,3,2}(x_1) & \gamma_{0,4}\psi_{0,4,2}(x_1) \\ \gamma_{0,1}\psi_{0,1,1}(x_2) & \gamma_{0,2}\psi_{0,2,1}(x_2) & \gamma_{0,3}\psi_{0,3,1}(x_2) & \gamma_{0,4}\psi_{0,4,1}(x_2) \\ \gamma_{0,1}\psi_{0,1,2}(x_2) & \gamma_{0,2}\psi_{0,2,2}(x_2) & \gamma_{0,3}\psi_{0,3,2}(x_2) & \gamma_{0,4}\psi_{0,4,2}(x_2) \end{pmatrix}$$

with the two spin components $\psi_{\zeta,\lambda,1}(x) = w_{\zeta,\lambda} \exp(i\gamma_{\zeta,\lambda}x)$ and $\psi_{\zeta,\lambda,2}(x) = d_{\zeta,\lambda} \exp(i\gamma_{\zeta,\lambda}x)$. Obviously, the nontrivial solution to Eq. (A13) requires

$$\det[\mathbf{M}(E)] = 0, \quad (\text{A14})$$

which yields an equation for the energy eigenvalues E , see Eqs. (A6) and (A7). Let E_{\uparrow} and E_{\downarrow} denote the two lowest energy solutions to Eq. (A14), with $E_{\uparrow} \geq E_{\downarrow}$. The explicit expressions for the two corresponding spinors can also be completely determined by the boundary conditions Eqs. (A11) in conjunction with the normalization condition $\int \Psi_{1,\tau=\uparrow,\downarrow}^\dagger(x)\Psi_{1,\tau}(x)dx = 1$, where $\tau = \uparrow, \downarrow$ indicate the two quasispin eigenstates on the dot.

The two lowest-energy spin states of the other quantum dot, QD2, i.e., $\Psi_{2,\uparrow}(x)$ and $\Psi_{2,\downarrow}(x)$, can be derived similarly to the discussion above. Due to the inversion symmetry which implies $V_{qd,1}(x) = V_{qd,2}(-x)$, the corresponding energy eigenvalues are identical to those of QD1.

Exploiting the localized wave functions on each quantum dot, we next derive the tunneling amplitudes of the double-quantum-dot (DQD) model, utilizing linear combinations of the atomic orbitals. The intracell amplitude is expediently found by considering the interdot tunneling in the double

$$\lim_{\epsilon \rightarrow 0} [\Psi_1'(x_1 + \epsilon) - \Psi_1'(x_1 - \epsilon)] = 0,$$

$$\lim_{\epsilon \rightarrow 0} [\Psi_1'(x_2 + \epsilon) - \Psi_1'(x_2 - \epsilon)] = 0. \quad (\text{A11})$$

By regarding $\hat{z}^T = \{c_{0,1}, c_{0,2}, c_{0,3}, c_{0,4}, c_{1,1}, c_{1,4}, c_{2,2}, c_{2,3}\}$ as the variable vector, Eq. (A11) can be written in a matrix form

$$\mathbf{M} \cdot \hat{z} = 0, \quad (\text{A12})$$

where

$$\begin{pmatrix} -\psi_{1,1,1}(x_1) & -\psi_{1,4,1}(x_1) & 0 & 0 \\ -\psi_{1,1,2}(x_1) & -\psi_{1,4,2}(x_1) & 0 & 0 \\ 0 & 0 & -\psi_{2,2,1}(x_2) & -\psi_{2,3,1}(x_2) \\ 0 & 0 & -\psi_{2,2,2}(x_2) & -\psi_{2,3,2}(x_2) \\ -\gamma_{1,1}\psi_{1,1,1}(x_1) & -\gamma_{1,4}\psi_{1,4,1}(x_1) & 0 & 0 \\ -\gamma_{1,1}\psi_{1,1,2}(x_1) & -\gamma_{1,4}\psi_{1,4,2}(x_1) & 0 & 0 \\ 0 & 0 & -\gamma_{2,2}\psi_{2,2,1}(x_2) & -\gamma_{2,3}\psi_{2,3,1}(x_2) \\ 0 & 0 & -\gamma_{2,2}\psi_{2,2,2}(x_2) & -\gamma_{2,3}\psi_{2,3,2}(x_2) \end{pmatrix}, \quad (\text{A13})$$

quantum-dot Hamiltonian [see Fig. 6(a)]

$$H_{\text{DQD-in}}(x) = \frac{p^2}{2m_e} + \alpha p\sigma_y + \frac{\Delta_z}{2}\sigma_z + V_{\text{DQD-in}}(x) - V_c, \quad (\text{A15})$$

with the double-well potential

$$V_{\text{DQD-in}}(x) = V_1[1 - \Theta(|x| - d)] + V_2\Theta(|x| - L + d) \quad (\text{A16})$$

and the constant chemical potential $V_c = \frac{1}{2}(E_{\uparrow} + E_{\downarrow})$ to offset the on-site orbital energy (which is conventionally set at zero for a prototype SSH model [4]). To this end, one first derives the orthonormal basis $\{\Phi_{1,\uparrow}(x), \Phi_{1,\downarrow}(x), \Phi_{2,\uparrow}(x), \Phi_{2,\downarrow}(x)\}$ using the four localized states $\Psi_{1/2,\uparrow}(x)$ and $\Psi_{1/2,\downarrow}(x)$. Those are then used to present the electron field operators as $\Psi_e(x) = \sum_{\sigma=\uparrow,\downarrow} [a_\sigma \Phi_{1,\sigma}(x) + b_\sigma \Phi_{2,\sigma}(x)]$, where a_σ (a_σ^\dagger) and b_σ (b_σ^\dagger) are the annihilation (creation) operators for the quasispin states on QD1 and QD2, respectively. The second quantized form of $H_{\text{DQD-in}}$ is then

$$H_{\text{DQD-in}} = \int \Psi_e^*(x)H_{\text{DQD-in}}(x)\Psi_e(x)dx \\ = \frac{\Delta_z}{2}(a^\dagger\sigma_z a + b^\dagger\sigma_z b) + (a^\dagger t_{\text{in}} b + \text{H.c.}), \quad (\text{A17})$$

with the spinors $a = \{a_\uparrow, a_\downarrow\}$ and $b = \{b_\uparrow, b_\downarrow\}$. In fact, the on-site energies of different quasispin states in each dot are modified by the spin-orbit interaction. However, as compared to the large spin-orbit length of the InAs nanowire, i.e., $x_{\text{so}} = 180$ nm, the small characteristic length of the dots, i.e., $L - 2d = 40$ nm, renders the spin-orbit interaction induced modification negligible, and then it is a good approximation to write the quasispin up (down) on-site energy as the positive (negative) half Zeeman splitting energy as in Eq. (A17). The quasispin tunneling amplitudes can be written as a matrix

$$t_{\text{in}} = t_{\text{in},0} \exp[i\varphi_{\text{in}}(\hat{\mathbf{v}}_{\text{in}} \cdot \hat{\boldsymbol{\sigma}})], \quad (\text{A18})$$

with

$$[t_{\text{in}}]_{\sigma\sigma'} = \int \Phi_{1,\sigma}^\dagger(x) H_{\text{DQD-in}} \Phi_{2,\sigma'}(x) dx. \quad (\text{A19})$$

As seen, the spin-orbit interaction appears as a (matrix) phase factor multiplying the intracell spin tunneling matrix. Here $t_{\text{in},0}$ is the real tunneling amplitude dominated by the potential difference $\Delta V = V_1 - V_2$ as shown in Fig. 6(c), φ_{in} is the spin rotation phase induced by the spin-orbit interaction, and $\hat{\mathbf{v}}_{\text{in}} = \{\sin(\vartheta_{\text{in}}), 0, \cos(\vartheta_{\text{in}})\}$ is the unit vector determining the direction of the axis of rotation. Numerically, φ_{in} is proportional to the ratio between the interdot distance and the spin-orbit length L/x_{so} with $x_{\text{so}} = \hbar/(m_e\alpha)$, and that is consistent with the analytical analysis in Ref. [37].

It is important to note that the coordinate system for defining the rotation vector $\hat{\mathbf{v}}_{\text{in}}$ does not coincide with that defining the spin operators in Eq. (A15). The x component of $\hat{\mathbf{v}}_{\text{in}}$ corresponds to the interdot spin-flip tunneling between the localized quasispin states, and vanishes in the absence of spin mixing. Therefore, for zero magnetic field, i.e., when $\Delta_z = 0$, or when $\theta = 0$, the vector $\hat{\mathbf{v}}_{\text{in}}$ is purely along the z direction since then $[H_{\text{DQD-in}}, \sigma_y] = 0$. In other cases, the specific value of ϑ_{in} depends on the degree of spin mixing on each localized quasispin state, which in turn is determined by the angle between the external magnetic field and the one induced by the spin-orbit interaction. The amplitude of the spin-flip tunneling in Eq. (A18), $t'_{\text{in}} = t_{\text{in},0} \sin(\varphi_{\text{in}}) \sin(\vartheta_{\text{in}})$, as a function of the tilting angle θ for a fixed magnitude of the magnetic field, is portrayed in Fig. 6(d), showing that it vanishes for $\theta = 0$.

The intercell hopping is addressed by considering a neighboring DQD [as shown in Fig. 6(b)] which obeys the Hamiltonian

$$H_{\text{DQD-ex}}(x) = \frac{p^2}{2m_e} + \alpha p\sigma_y + \frac{\Delta_z}{2}\sigma_\zeta + V_{\text{DQD-ex}}(x) - V_c, \quad (\text{A20})$$

where the double-well potential takes the form

$$V_{\text{DQD-ex}}(x) = V_2[1 - \Theta(|x| - d)] + V_1\Theta(|x| - L + d). \quad (\text{A21})$$

Similar to the intracell spin tunneling discussed above, the spin transfer matrix for the intercell tunneling takes the form

$$t_{\text{ex}} = t_{\text{ex},0} \exp[i\varphi_{\text{ex}}(\hat{\mathbf{v}}_{\text{ex}} \cdot \hat{\boldsymbol{\sigma}})], \quad (\text{A22})$$

with $t_{\text{ex},0}$ and φ_{ex} corresponding to the real amplitude and the spin rotation phase of the interdot tunneling, and $\hat{\mathbf{v}}_{\text{ex}} = \{\sin(\vartheta_{\text{ex}}), 0, \cos(\vartheta_{\text{ex}})\}$ describing the direction of the axis

of rotation. Analogously, the corresponding spin-flip tunneling amplitude $t'_{\text{ex}} = t_{\text{ex},0} \sin(\varphi_{\text{ex}}) \sin(\vartheta_{\text{ex}})$ can be regulated by manipulating the tilting angle θ , as shown in Fig. 6(d). Introducing the intracell spin tunneling, the second quantized Hamiltonian of the double-quantum-dot chain is

$$H_T = \sum_n \frac{\Delta_z}{2} (a_n^\dagger \sigma_z a_n + b_n^\dagger \sigma_z b_n) + \sum_n (a_n^\dagger t_{\text{in}} b_n + a_{n+1}^\dagger t_{\text{ex}} b_n + \text{H.c.}), \quad (\text{A23})$$

where n is the index of the unit cell, and $a_n = \{a_{n\uparrow}, a_{n\downarrow}\}$ and $b_n = \{b_{n\uparrow}, b_{n\downarrow}\}$ are spinors.

For a spinless DQD chain, the tunneling matrices in Eqs. (A18) and (A22) become real numbers, $t_{\text{in},0}$ and $t_{\text{ex},0}$, and the effective tight-binding Hamiltonian is identical to that of the single-level Su-Schrieffer-Heeger model [4]

$$H_{T,0} = \sum_n (t_{\text{in},0} a_n^\dagger b_n + t_{\text{ex},0} a_{n+1}^\dagger b_n + \text{H.c.}), \quad (\text{A24})$$

with a_n and b_n corresponding to the operators for the lowest localized orbitals on the QD1 and QD2, respectively.

APPENDIX B: THE BLOCH SPECTRUM OF THE DOUBLE-QUANTUM-DOT CHAIN

Here the detailed calculation of the Bloch bands of our system is given. For a one-dimensional lattice obeying periodic boundary conditions, the eigenstates are the Bloch wave functions

$$\Psi_k(x) = \exp(ikx)u_k(x), \quad (\text{B1})$$

where k is the wave vector and $u_k(x)$ is the cell-periodic Bloch wave function. Obviously, the corresponding energy spectrum $\varepsilon(k)$ is given by

$$H\Psi_k(x) = \varepsilon(k)\Psi_k(x), \quad (\text{B2})$$

where

$$H = \frac{p^2}{2m_e} - V_c + U(x) + \alpha p\sigma_y + \frac{\Delta_z}{2}\sigma_\zeta. \quad (\text{B3})$$

Similarly to the derivation in Appendix A, the solutions of Eq. (B2) are obtained from the eigenfunctions of the Schrödinger equations with different gate potentials

$$\tilde{H}_{\zeta=0,1,2}\Psi_{k,\zeta}(x) = E\Psi_{k,\zeta}(x). \quad (\text{B4})$$

where $\Psi_{k,\zeta}(x) = \exp(ikx)u_{k,\zeta}(x)$ and $\varepsilon(k) = E - V_c$ (measured from the chemical potential V_c). Then, analogously to the eigenstates in Eq. (A4), there exist fourfold degenerate solutions to Eq. (B4) for a fixed k , of the form

$$u_{k,\zeta,\lambda}(x) = \exp[i(\gamma_{\zeta,\lambda} - k)x] \begin{pmatrix} w_{\zeta,\lambda} \\ d_{\zeta,\lambda} \end{pmatrix} \quad (\text{B5})$$

with the wave vector $\gamma_{\zeta,\lambda}$ and the two spin components ($u_{\zeta,\lambda}$ and $d_{\zeta,\lambda}$) determined by Eqs. (A6) and (A7). It is convenient to divide the unit cell into four parts, as shown in Fig. 7.

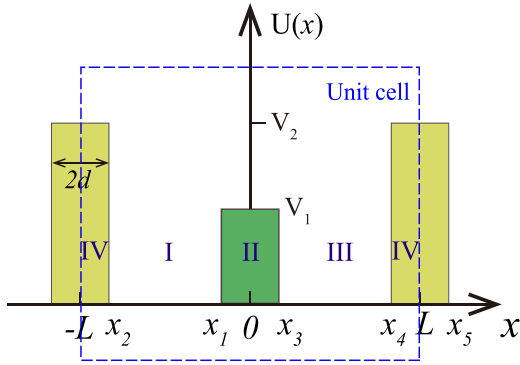


FIG. 7. The spatial distribution of the confinement potential $U(x)$ in a unit cell; the separation of the unit cell into four regions (denoted by I, II, III, and IV) in which the Bloch functions are derived (see text).

The Bloch functions in each segment are expanded as

$$\begin{aligned}
 u_{k,I}(x) &= \sum_{\lambda=1}^4 c_{I,\lambda} u_{k,0,\lambda}(x) \\
 u_{k,II}(x) &= \sum_{\lambda=1}^4 c_{II,\lambda} u_{k,1,\lambda}(x) \\
 u_{k,III}(x) &= \sum_{\lambda=1}^4 c_{III,\lambda} u_{k,0,\lambda}(x) \\
 u_{k,IV}(x) &= \sum_{\lambda=1}^4 c_{IV,\lambda} u_{k,2,\lambda}(x), \quad (B6)
 \end{aligned}$$

with $c_{\Lambda,\lambda}$ ($\Lambda = I, II, III, IV$) representing the, yet to be determined, 16 coefficients. The entire Bloch wave function is then

$$\begin{aligned}
 u_k(x) &= \Theta(x + L - d)[1 - \Theta(x + d)]u_{k,I}(x) + [1 - \Theta(|x| - d)]u_{k,II}(x) + [1 - \Theta(x - L + d)] \\
 &\quad \times \Theta(x - d)u_{k,III}(x) + \Theta(|x| - L + d)[1 - \Theta(|x| - L)]u_{k,IV}(x). \quad (B7)
 \end{aligned}$$

Combined with the periodicity of the cell Bloch functions, i.e., $u_k(x_2) = u_k(x_5)$ and $u'_k(x_2) = u'_k(x_5)$ with $x_5 \equiv x_2 + 2L = L + d$, the energy bands are determined by the continuity of the wave function at the interfaces, $\lim_{\epsilon \rightarrow 0}[u_k(\xi + \epsilon) - u_k(\xi - \epsilon)] = 0$ and $\lim_{\epsilon \rightarrow 0}[u'_k(\xi + \epsilon) - u'_k(\xi - \epsilon)] = 0$, with $\xi = x_1, x_3, x_4$. Regarding the coefficients of the combinations in Eqs. (B6) as a variable vector, the prerequisite conditions can be written in a matrix form

$$\mathbf{W}(k, E) \cdot \hat{\delta} = 0, \quad (B8)$$

where the vector is $\hat{\delta}^T = \{c_{I,1}, c_{I,2}, c_{I,3}, c_{I,4}, c_{II,1}, c_{II,2}, c_{II,3}, c_{II,4}, c_{III,1}, c_{III,2}, c_{III,3}, c_{III,4}, c_{IV,1}, c_{IV,2}, c_{IV,3}, c_{IV,4}\}$ and the matrix is

$$\mathbf{W} = \begin{pmatrix}
 u_{k,0,\lambda}^{(1,\uparrow)} & u_{k,0,\lambda}^{(1,\uparrow)} & u_{k,0,\lambda}^{(1,\uparrow)} & u_{k,0,\lambda}^{(1,\uparrow)} & -u_{k,1,\lambda}^{(1,\uparrow)} & -u_{k,1,\lambda}^{(1,\uparrow)} & -u_{k,1,\lambda}^{(1,\uparrow)} & -u_{k,1,\lambda}^{(1,\uparrow)} & 0 & 0 & 0 & 0 & 0 & 0 & 0 & 0 & 0 & 0 \\
 u_{k,0,\lambda}^{(1,\downarrow)} & u_{k,0,\lambda}^{(1,\downarrow)} & u_{k,0,\lambda}^{(1,\downarrow)} & u_{k,0,\lambda}^{(1,\downarrow)} & -u_{k,1,\lambda}^{(1,\downarrow)} & -u_{k,1,\lambda}^{(1,\downarrow)} & -u_{k,1,\lambda}^{(1,\downarrow)} & -u_{k,1,\lambda}^{(1,\downarrow)} & 0 & 0 & 0 & 0 & 0 & 0 & 0 & 0 & 0 & 0 \\
 0 & 0 & 0 & 0 & -u_{k,1,\lambda}^{(3,\uparrow)} & -u_{k,1,\lambda}^{(3,\uparrow)} & -u_{k,1,\lambda}^{(3,\uparrow)} & -u_{k,1,\lambda}^{(3,\uparrow)} & u_{k,0,\lambda}^{(3,\uparrow)} & u_{k,0,\lambda}^{(3,\uparrow)} & u_{k,0,\lambda}^{(3,\uparrow)} & u_{k,0,\lambda}^{(3,\uparrow)} & 0 & 0 & 0 & 0 & 0 \\
 0 & 0 & 0 & 0 & -u_{k,1,\lambda}^{(3,\downarrow)} & -u_{k,1,\lambda}^{(3,\downarrow)} & -u_{k,1,\lambda}^{(3,\downarrow)} & -u_{k,1,\lambda}^{(3,\downarrow)} & u_{k,0,\lambda}^{(3,\downarrow)} & u_{k,0,\lambda}^{(3,\downarrow)} & u_{k,0,\lambda}^{(3,\downarrow)} & u_{k,0,\lambda}^{(3,\downarrow)} & 0 & 0 & 0 & 0 & 0 \\
 0 & 0 & 0 & 0 & 0 & 0 & 0 & 0 & u_{k,0,\lambda}^{(4,\uparrow)} & u_{k,0,\lambda}^{(4,\uparrow)} & u_{k,0,\lambda}^{(4,\uparrow)} & u_{k,0,\lambda}^{(4,\uparrow)} & -u_{k,2,\lambda}^{(4,\uparrow)} & -u_{k,2,\lambda}^{(4,\uparrow)} & -u_{k,2,\lambda}^{(4,\uparrow)} & -u_{k,2,\lambda}^{(4,\uparrow)} & -u_{k,2,\lambda}^{(4,\uparrow)} \\
 0 & 0 & 0 & 0 & 0 & 0 & 0 & 0 & u_{k,0,\lambda}^{(4,\downarrow)} & u_{k,0,\lambda}^{(4,\downarrow)} & u_{k,0,\lambda}^{(4,\downarrow)} & u_{k,0,\lambda}^{(4,\downarrow)} & -u_{k,2,\lambda}^{(4,\downarrow)} & -u_{k,2,\lambda}^{(4,\downarrow)} & -u_{k,2,\lambda}^{(4,\downarrow)} & -u_{k,2,\lambda}^{(4,\downarrow)} & -u_{k,2,\lambda}^{(4,\downarrow)} \\
 u_{k,0,\lambda}^{(2,\uparrow)} & u_{k,0,\lambda}^{(2,\uparrow)} & u_{k,0,\lambda}^{(2,\uparrow)} & u_{k,0,\lambda}^{(2,\uparrow)} & 0 & 0 & 0 & 0 & 0 & 0 & 0 & 0 & -u_{k,2,\lambda}^{(5,\uparrow)} & -u_{k,2,\lambda}^{(5,\uparrow)} & -u_{k,2,\lambda}^{(5,\uparrow)} & -u_{k,2,\lambda}^{(5,\uparrow)} & -u_{k,2,\lambda}^{(5,\uparrow)} \\
 u_{k,0,\lambda}^{(2,\downarrow)} & u_{k,0,\lambda}^{(2,\downarrow)} & u_{k,0,\lambda}^{(2,\downarrow)} & u_{k,0,\lambda}^{(2,\downarrow)} & 0 & 0 & 0 & 0 & 0 & 0 & 0 & 0 & -u_{k,2,\lambda}^{(5,\downarrow)} & -u_{k,2,\lambda}^{(5,\downarrow)} & -u_{k,2,\lambda}^{(5,\downarrow)} & -u_{k,2,\lambda}^{(5,\downarrow)} & -u_{k,2,\lambda}^{(5,\downarrow)} \\
 \tilde{u}_{k,0,\lambda}^{(1,\uparrow)} & \tilde{u}_{k,0,\lambda}^{(1,\uparrow)} & \tilde{u}_{k,0,\lambda}^{(1,\uparrow)} & \tilde{u}_{k,0,\lambda}^{(1,\uparrow)} & -\tilde{u}_{k,1,\lambda}^{(1,\uparrow)} & -\tilde{u}_{k,1,\lambda}^{(1,\uparrow)} & -\tilde{u}_{k,1,\lambda}^{(1,\uparrow)} & -\tilde{u}_{k,1,\lambda}^{(1,\uparrow)} & 0 & 0 & 0 & 0 & 0 & 0 & 0 & 0 & 0 & 0 \\
 \tilde{u}_{k,0,\lambda}^{(1,\downarrow)} & \tilde{u}_{k,0,\lambda}^{(1,\downarrow)} & \tilde{u}_{k,0,\lambda}^{(1,\downarrow)} & \tilde{u}_{k,0,\lambda}^{(1,\downarrow)} & -\tilde{u}_{k,1,\lambda}^{(1,\downarrow)} & -\tilde{u}_{k,1,\lambda}^{(1,\downarrow)} & -\tilde{u}_{k,1,\lambda}^{(1,\downarrow)} & -\tilde{u}_{k,1,\lambda}^{(1,\downarrow)} & 0 & 0 & 0 & 0 & 0 & 0 & 0 & 0 & 0 & 0 \\
 0 & 0 & 0 & 0 & -\tilde{u}_{k,1,\lambda}^{(3,\uparrow)} & -\tilde{u}_{k,1,\lambda}^{(3,\uparrow)} & -\tilde{u}_{k,1,\lambda}^{(3,\uparrow)} & -\tilde{u}_{k,1,\lambda}^{(3,\uparrow)} & \tilde{u}_{k,0,\lambda}^{(3,\uparrow)} & \tilde{u}_{k,0,\lambda}^{(3,\uparrow)} & \tilde{u}_{k,0,\lambda}^{(3,\uparrow)} & \tilde{u}_{k,0,\lambda}^{(3,\uparrow)} & 0 & 0 & 0 & 0 & 0 \\
 0 & 0 & 0 & 0 & -\tilde{u}_{k,1,\lambda}^{(3,\downarrow)} & -\tilde{u}_{k,1,\lambda}^{(3,\downarrow)} & -\tilde{u}_{k,1,\lambda}^{(3,\downarrow)} & -\tilde{u}_{k,1,\lambda}^{(3,\downarrow)} & \tilde{u}_{k,0,\lambda}^{(3,\downarrow)} & \tilde{u}_{k,0,\lambda}^{(3,\downarrow)} & \tilde{u}_{k,0,\lambda}^{(3,\downarrow)} & \tilde{u}_{k,0,\lambda}^{(3,\downarrow)} & 0 & 0 & 0 & 0 & 0 \\
 0 & 0 & 0 & 0 & 0 & 0 & 0 & 0 & \tilde{u}_{k,0,\lambda}^{(4,\uparrow)} & \tilde{u}_{k,0,\lambda}^{(4,\uparrow)} & \tilde{u}_{k,0,\lambda}^{(4,\uparrow)} & \tilde{u}_{k,0,\lambda}^{(4,\uparrow)} & -\tilde{u}_{k,2,\lambda}^{(4,\uparrow)} & -\tilde{u}_{k,2,\lambda}^{(4,\uparrow)} & -\tilde{u}_{k,2,\lambda}^{(4,\uparrow)} & -\tilde{u}_{k,2,\lambda}^{(4,\uparrow)} & -\tilde{u}_{k,2,\lambda}^{(4,\uparrow)} \\
 0 & 0 & 0 & 0 & 0 & 0 & 0 & 0 & \tilde{u}_{k,0,\lambda}^{(4,\downarrow)} & \tilde{u}_{k,0,\lambda}^{(4,\downarrow)} & \tilde{u}_{k,0,\lambda}^{(4,\downarrow)} & \tilde{u}_{k,0,\lambda}^{(4,\downarrow)} & -\tilde{u}_{k,2,\lambda}^{(4,\downarrow)} & -\tilde{u}_{k,2,\lambda}^{(4,\downarrow)} & -\tilde{u}_{k,2,\lambda}^{(4,\downarrow)} & -\tilde{u}_{k,2,\lambda}^{(4,\downarrow)} & -\tilde{u}_{k,2,\lambda}^{(4,\downarrow)} \\
 \tilde{u}_{k,0,\lambda}^{(2,\uparrow)} & \tilde{u}_{k,0,\lambda}^{(2,\uparrow)} & \tilde{u}_{k,0,\lambda}^{(2,\uparrow)} & \tilde{u}_{k,0,\lambda}^{(2,\uparrow)} & 0 & 0 & 0 & 0 & 0 & 0 & 0 & 0 & -\tilde{u}_{k,2,\lambda}^{(5,\uparrow)} & -\tilde{u}_{k,2,\lambda}^{(5,\uparrow)} & -\tilde{u}_{k,2,\lambda}^{(5,\uparrow)} & -\tilde{u}_{k,2,\lambda}^{(5,\uparrow)} & -\tilde{u}_{k,2,\lambda}^{(5,\uparrow)} \\
 \tilde{u}_{k,0,\lambda}^{(2,\downarrow)} & \tilde{u}_{k,0,\lambda}^{(2,\downarrow)} & \tilde{u}_{k,0,\lambda}^{(2,\downarrow)} & \tilde{u}_{k,0,\lambda}^{(2,\downarrow)} & 0 & 0 & 0 & 0 & 0 & 0 & 0 & 0 & -\tilde{u}_{k,2,\lambda}^{(5,\downarrow)} & -\tilde{u}_{k,2,\lambda}^{(5,\downarrow)} & -\tilde{u}_{k,2,\lambda}^{(5,\downarrow)} & -\tilde{u}_{k,2,\lambda}^{(5,\downarrow)} & -\tilde{u}_{k,2,\lambda}^{(5,\downarrow)}
 \end{pmatrix} \quad (B9)$$

with $u_{k,\zeta,\lambda}^{(j,\uparrow)} = \exp[i(\gamma_{\zeta,\lambda} - k)x_j]w_{\zeta,\lambda}$ ($j = 1, 2, 3, 4, 5$), $u_{k,\zeta,\lambda}^{(j,\downarrow)} = \exp[i(\gamma_{\zeta,\lambda} - k)x_j]d_{\zeta,\lambda}$, $\tilde{u}_{k,\zeta,\lambda}^{(j,\uparrow)} = (\gamma_{\zeta,\lambda} - k) \exp[i(\gamma_{\zeta,\lambda} - k)x_j]w_{\zeta,\lambda}$, and $\tilde{u}_{k,\zeta,\lambda}^{(j,\downarrow)} = (\gamma_{\zeta,\lambda} - k) \exp[i(\gamma_{\zeta,\lambda} - k)x_j]d_{\zeta,\lambda}$. A nontrivial solution to Eq. (B8) requires

$$\det[\mathbf{W}(k, E)] = 0, \quad (B10)$$

and yields an implicit equation for k and E of Eqs. (A6), (A7), and (B9). The exact energy spectrum of the Bloch band

$\varepsilon(k) = E - V_c$ is found by solving numerically for E at a fixed value of k . Substituting the so-derived values of E in Eq. (B8) yields the values of the coefficients $c_{\Lambda,\lambda}$, i.e., gives the specific form of the Bloch wave functions, with the normalization condition $\int_{-L}^L u_k^*(x)u_k(x)dx = 1$.

In the absence of a magnetic field or when $\theta = 0$, the two spin degrees of freedom are separable and the number of the corresponding coefficients for ascertaining the Bloch band is reduced by half, which is similar to a spinless chain.

In this case, the matrix $\mathbf{W}(k, E)$ is decomposed into two independent submatrices whose determinants yield the Bloch

spectrum, as shown in Fig. 2(c) for the case of zero magnetic field.

-
- [1] J. E. Moore, The birth of topological insulators, *Nature (London)* **464**, 194 (2010).
- [2] M. Z. Hasan and C. L. Kane, Colloquium: Topological insulators, *Rev. Mod. Phys.* **82**, 3045 (2010).
- [3] S. Ryu and Y. Hatsugai, Topological Origin of Zero-Energy Edge States in Particle-Hole Symmetric Systems, *Phys. Rev. Lett.* **89**, 077002 (2002); T. Kawarabayashi and Y. Hatsugai, Bulk-edge correspondence with generalized chiral symmetry, *Phys. Rev. B* **103**, 205306 (2021).
- [4] W. P. Su, J. R. Schrieffer, and A. J. Heeger, Solitons in Polyacetylene, *Phys. Rev. Lett.* **42**, 1698 (1979).
- [5] M. J. Rice and E. J. Mele, Elementary Excitations of a Linearly Conjugated Diatomic Polymer, *Phys. Rev. Lett.* **49**, 1455 (1982).
- [6] L. Li, Z. Xu, and S. Chen, Topological phases of generalized Su-Schrieffer-Heeger models, *Phys. Rev. B* **89**, 085111 (2014).
- [7] D. Xie, W. Gou, T. Xiao, B. Gadway, and B. Yan, Topological characterizations of an extended Su-Schrieffer-Heeger model, *npj Quantum Inf.* **5**, 55 (2019).
- [8] B. Zhu, R. Lu, and S. Chen, PT symmetry in the non-Hermitian Su-Schrieffer-Heeger model with complex boundary potentials, *Phys. Rev. A* **89**, 062102 (2014).
- [9] S. Lieu, Topological phases in the non-Hermitian Su-Schrieffer-Heeger model, *Phys. Rev. B* **97**, 045106 (2018).
- [10] F. K. Kunst, E. Edvardsson, J. C. Budich, and E. J. Bergholtz, Biorthogonal Bulk-Boundary Correspondence in Non-Hermitian Systems, *Phys. Rev. Lett.* **121**, 026808 (2018).
- [11] S. Yao and Z. Wang, Edge States and Topological Invariants of Non-Hermitian Systems, *Phys. Rev. Lett.* **121**, 086803 (2018).
- [12] R. Chen, C.-Z. Chen, B. Zhou, and D.-H. Xu, Finite-size effects in non-Hermitian topological systems, *Phys. Rev. B* **99**, 155431 (2019).
- [13] L.-J. Lang, X. Cai, and S. Chen, Edge States and Topological Phases in One-Dimensional Optical Superlattices, *Phys. Rev. Lett.* **108**, 220401 (2012).
- [14] M. Atala, M. Aidelsburger, J. T. Barreiro, D. Abanin, T. Kitagawa, E. Demler, and I. Bloch, Direct measurement of the Zak phase in topological Bloch bands, *Nat. Phys.* **9**, 795 (2013).
- [15] E. J. Meier, F. Alex An, and B. Gadway, Observation of the topological soliton state in the Su-Schrieffer-Heeger model, *Nat. Commun.* **7**, 13986 (2016).
- [16] M. Leder, C. Grossert, L. Sitta, M. Genske, A. Rosch, and M. Weitz, Real-space imaging of a topologically protected edge state with ultracold atoms in an amplitude-chirped optical lattice, *Nat. Commun.* **7**, 13112 (2016).
- [17] D. D. Solnyshkov, A. V. Nalitimov, and G. Malpuech, Kibble-Zurek Mechanism in Topologically Nontrivial Zigzag Chains of Polariton Micropillars, *Phys. Rev. Lett.* **116**, 046402 (2016).
- [18] P. St-Jean, V. Goblot, E. Galopin, A. Lemaître, T. Ozawa, L. Le Gratiet, I. Sagnes, J. Bloch, and A. Amo, Lasing in topological edge states of a one-dimensional lattice, *Nat. Photon.* **11**, 651 (2017).
- [19] M. Parto, S. Wittek, H. Hodaei, G. Harari, M. A. Bandres, J. Ren, M. C. Rechtsman, M. Segev, D. N. Christodoulides, and M. Khajavikhan, Edge-Mode Lasing in 1D Topological Active Arrays, *Phys. Rev. Lett.* **120**, 113901 (2018).
- [20] C. E. Whittaker, E. Cancellieri, P. M. Walker, B. Royall, L. E. Tapia Rodríguez, E. Clarke, D. M. Whittaker, H. Schomerus, M. S. Skolnick, and D. N. Krizhanovskii, Effect of photonic spin-orbit coupling on the topological edge modes of a Su-Schrieffer-Heeger chain, *Phys. Rev. B* **99**, 081402(R) (2019).
- [21] O. Gröning, S. Wang, X. Yao, C. A. Pignedoli, G. B. Barin, C. Daniels, A. Cupo, V. Meunier, X. Feng, A. Narita, K. Müllen, P. Ruffieux, and R. Fasel, Engineering of robust topological quantum phases in graphene nanoribbons, *Nature* **560**, 209 (2018).
- [22] R. Drost, T. Ojanen, A. Harju, and P. Liljeroth, Topological states in engineered atomic lattices, *Nat. Phys.* **13**, 668 (2017).
- [23] D. J. Rizzo, G. Veber, T. Cao, C. Bronner, T. Chen, F. Zhao, H. Rodriguez, S. G. Louie, M. F. Crommie, and F. R. Fischer, Topological band engineering of graphene nanoribbons, *Nature* **560**, 204 (2018).
- [24] C. L. Kane and E. J. Mele, Z_2 Topological Order and the Quantum Spin Hall Effect, *Phys. Rev. Lett.* **95**, 146802 (2005); Quantum Spin Hall Effect in Graphene, **95**, 226801 (2005).
- [25] J. D. Sau, R. M. Lutchyn, S. Tewari, and S. Das Sarma, Generic New Platform for Topological Quantum Computation Using Semiconductor Heterostructures, *Phys. Rev. Lett.* **104**, 040502 (2010).
- [26] Z. Yan and S. Wan, Topological phases, topological flat bands, and topological excitations in a one-dimensional dimerized lattice with spin-orbit coupling, *Europhys. Lett.* **107**, 47007 (2014).
- [27] M. Bahari and M. V. Hosseini, Zeeman-field-induced nontrivial topological phases in a one-dimensional spin-orbit-coupled dimerized lattice, *Phys. Rev. B* **94**, 125119 (2016).
- [28] Y. Aharonov and A. Casher, Topological Quantum Effects for Neutral Particles, *Phys. Rev. Lett.* **53**, 319 (1984).
- [29] Y. Yao, M. Sato, T. Nakamura, N. Furukawa, and M. Oshikawa, Theory of electron spin resonance in one-dimensional topological insulators with spin-orbit couplings: Detection of edge states, *Phys. Rev. B* **96**, 205424 (2017).
- [30] T. V. Shahbazyan and M. E. Raikh, Low-Field Anomaly in 2D Hopping Magnetoresistance Caused by Spin-Orbit Term in the Energy Spectrum, *Phys. Rev. Lett.* **73**, 1408 (1994); O. Entin-Wohlman and A. Aharony, DC Spin geometric phases in hopping magnetoconductance, *Phys. Rev. Research* **1**, 033112 (2019).
- [31] W.-F. Zhang, C.-Y. Li, X.-F. Chen, C.-M. Huang, and F.-W. Ye, Topological zero-energy modes in time-reversal-symmetry-broken systems, *Acta Phys. Sin.* **66**, 220201 (2017).
- [32] F. Grusdt, M. Hönig, and M. Fleischhauer, Topological Edge States in the One-Dimensional Superlattice Bose-Hubbard Model, *Phys. Rev. Lett.* **110**, 260405 (2013).
- [33] Z.-H. Liu, R. Li, X. Hu, and J. Q. You, Spin-orbit coupling and electric-dipole spin resonance in a nanowire double quantum dot, *Sci. Rep.* **8**, 2302 (2018).

- [34] R. Winkler, *Spin-orbit Coupling Effects in Two-dimensional Electron and Hole Systems* (Springer, Berlin, 2003).
- [35] Z. Scherübl, G. Fülöp, M. H. Madsen, J. Nygård, and S. Csonka, Electrical tuning of Rashba spin-orbit interaction in multigated InAs nanowires, *Phys. Rev. B* **94**, 035444 (2016).
- [36] The sum of the two periodic barrier potentials is fixed as 40 meV to ensure effective coupling between two adjacent dots when manipulating the dimerization strength, scaled by the potential difference $\Delta V = V_1 - V_2$.
- [37] Z.-H. Liu, O. Entin-Wohlman, A. Aharony, and J. Q. You, Control of the two-electron exchange interaction in a nanowire double quantum dot, *Phys. Rev. B* **98**, 241303(R) (2018).
- [38] P. Delplace, D. Ullmo, and G. Montambaux, Zak phase and the existence of edge states in graphene, *Phys. Rev. B* **84**, 195452 (2011).
- [39] The consistency between the continuous Hamiltonian [see Eq. (1)] and the discrete model in Eq. (3) requires the conditions $L \gg 4d$ and $\min\{V_1, V_2\} \gg \max\{\Delta_z, m_e \alpha^2\}$.
- [40] J. Zak, Berry's Phase for Energy Bands in Solids, *Phys. Rev. Lett.* **62**, 2747 (1989).
- [41] Y. Hatsugai, Quantized Berry phases as a local order parameter of a quantum liquid, *J. Phys. Soc. Jpn.* **75**, 123601 (2006).
- [42] T. Fukui, Y. Hatsugai, and H. Suzuki, Chern numbers in discretized Brillouin zone: Efficient method of computing (spin) Hall conductances, *J. Phys. Soc. Jpn.* **74**, 1674 (2005).
- [43] J. K. Asbóthe, L. Oroszlány, and A. Pályi, The Su-Schrieffer-Heeger (SSH) model, *Lect. Notes Phys.* **919**, 1 (2016).
- [44] P. Nevado, S. Fernández-Lorenzo, and D. Porrás, Topological Edge States in Periodically Driven Trapped-Ion Chains, *Phys. Rev. Lett.* **119**, 210401 (2017).
- [45] R. Li, J. Q. You, C. P. Sun, and F. Nori, Controlling a Nanowire Spin-Orbit Qubit Via Electric-Dipole Spin Resonance, *Phys. Rev. Lett.* **111**, 086805 (2013).
- [46] H. A. Nilsson, P. Caroff, C. Thelander, M. Larsson, J. B. Wagner, L.-E. Wernersson, L. Samuelson, and H. Q. Xu, Giant, level-dependent g factors in InSb nanowire quantum dots, *Nano. Lett.* **9**, 3151 (2009).
- [47] J. Mu, S. Huang, Z.-H. Liu, W. Li, J.-Y. Wang, D. Pan, G.-Y. Huang, Y. Chen, J. Zhao, and H. Q. Xu, A highly tunable quadruple quantum dot in a narrow bandgap semiconductor InAs nanowire, *Nanoscale* **13**, 3983 (2021).
- [48] D. Jong, J. Veen, L. Binci, A. Singh, P. Krogstrup, L. P. Kouwenhoven, W. Pfaff, and J. D. Watson, Rapid Detection of Coherent Tunneling in an InAs Nanowire Quantum Dot Through Dispersive Gate Sensing, *Phy. Rev. Appl.* **11**, 044061 (2019).
- [49] Note that the effective magnetic field induced by the spin-orbit interaction is perpendicular to the chain. Consequently, the boundary conditions along the chain involve the momentum (i.e., the derivative with respect to x) and not the covariant momentum.